Monthly Notices
of the
ROYAL ASTRONOMICAL SOCIETY

MNRAS **443,** 3463–3476 (2014) doi:10.1093/mnras/stu1307

In a hot bubble: why does superbubble feedback work, but isolated supernovae do not?

Prateek Sharma,[1⋆] Arpita Roy,[1,2] Biman B. Nath[2] and Yuri Shchekinov[3]

[1]*Joint Astronomy Programme and Department of Physics, Indian Institute of Science, Bangalore 560012, India*
[2]*Raman Research Institute, Sadashiva Nagar, Bangalore 560080, India*
[3]*Department of Physics, Southern Federal University, Rostov on Don 344090, Russia*

Accepted 2014 July 27. Received 2014 June 12; in original form 2014 February 25

ABSTRACT

Using idealized one-dimensional Eulerian hydrodynamic simulations, we contrast the behaviour of isolated supernovae with the superbubbles driven by multiple, collocated supernovae. Continuous energy injection via successive supernovae exploding within the hot/dilute bubble maintains a strong termination shock. This strong shock keeps the superbubble overpressured and drives the outer shock well after it becomes radiative. Isolated supernovae, in contrast, with no further energy injection, become radiative quite early ($\lesssim$0.1 Myr, tens of pc), and stall at scales $\lesssim$100 pc. We show that isolated supernovae lose almost all of their mechanical energy by 1 Myr, but superbubbles can retain up to ∼40 per cent of the input energy in the form of mechanical energy over the lifetime of the star cluster (a few tens of Myr). These conclusions hold even in the presence of realistic magnetic fields and thermal conduction. We also compare various methods for implementing supernova feedback in numerical simulations. For various feedback prescriptions, we derive the spatial scale below which the energy needs to be deposited in order for it to couple to the interstellar medium. We show that a steady thermal wind within the superbubble appears only for a large number ($\gtrsim 10^4$) of supernovae. For smaller clusters, we expect multiple internal shocks instead of a smooth, dense thermalized wind.

Key words: shock waves – ISM: bubbles – ISM: supernova remnants – galaxies: ISM.

1 INTRODUCTION

Gravity and dark energy govern the structure in the Universe at the largest scales but complex baryonic processes, such as cooling, heating, self-gravity and star formation, are important at galactic scales (e.g. Springel et al. 2005). Numerical simulations have allowed us to make tremendous progress in our understanding of galaxy formation, from pure gravitational *N*-body simulations to the current models that try to model the aforementioned complex processes. Modelling the gravitationally interacting dark matter is straightforward in principle, and only limited by the available computing power. However, the modelling of baryonic processes is rather involved. In particular, there is no consensus on which baryonic processes are important and how they should be implemented numerically. Given the dynamic range of scales, from large-scale structure (tens of Mpc) to an individual star-forming cloud (∼pc), simulations have to resort to unresolved 'subgrid' models for star formation and feedback as a result of star formation (e.g. Navarro & White 1993; Gerritsen 1997; Springel & Hernquist 2003; Guedes et al. 2011; Hopkins, Quataert & Murray 2012 and references therein). While different star formation simulations seem to give similar star formation histories and stellar mass distributions, provided molecular clouds are resolved (e.g. Hopkins, Quataert & Murray 2011), the simulations are quite sensitive to the various feedback prescriptions (e.g. thermal feedback due to supernovae, momentum injection via dust absorbing/scattering photons produced by massive stars and supernovae), even with high resolution.

Stars form in clusters and superstar clusters (hundreds to 10^6 stars) of various sizes and in different environments, ranging from low-density galactic outskirts to dense galactic centres (see Portegies Zwart et al. 2010 for a review). These clusters are observed to disrupt the dense molecular clouds in which they are born (e.g. Leisawitz, Bash & Thaddeus 1989; Zhang, Fall & Whitmore 2001). This stellar feedback (resulting from strong radiation, stellar winds and supernovae) disperses cold gas and suppresses further star formation. Because of the stellar initial mass function (IMF) and the main-sequence lifetimes, the energy input is roughly constant per unit time over the lifetime of stars more massive than $8\,M_\odot$ (∼50 Myr; McCray & Kafatos 1987). Therefore, stellar feedback is sometimes modelled as a constant luminosity-driven blast wave (Weaver et al. 1977; Mac Low, McCray & Norman 1989;

⋆ E-mail: prateek@physics.iisc.ernet.in

© 2014 The Authors
Published by Oxford University Press on behalf of the Royal Astronomical Society

Gerritsen 1997). A superbubble (SB) expands faster than an isolated supernova remnant (SNR) because of continuous energy injection, and suffers smaller cooling losses because most supernovae (SNe) explode in a low-density bubble.

The hot bubble breaks out through the gas disc if the outer shock driven by overlapping SNe crosses the scaleheight with a sufficient Mach number within the starburst lifetime (e.g. see section 2 of Roy et al. 2013). After breakout, the hot, metal-rich stellar ejecta are spread out into the galactic halo via the Rayleigh–Taylor instability. The spread of metals over large scales is required to explain the high metallicity observed in the intergalactic medium (IGM), far away from the stellar disc (Tumlinson et al. 2011).

Standard models for feedback through multiple SNe assume that a fraction $\gtrsim$0.3 of the total explosion energy is retained in the hot interstellar medium (ISM; e.g. Strickland & Heckman 2009). This fraction is much larger than the estimates for a single SNR ($\sim$0.1) after the radiative phase at $\lesssim$0.1 Myr (e.g. Cox 1972; Chevalier 1974; Thornton et al. 1998, hereafter T98). Moreover, there are further radiative and adiabatic losses, such that over the time-scale of the order of tens of Myr, the available mechanical energy in the bubble and shell is a negligible ($\ll$0.1) fraction of the initial SN energy input. Recently, Nath & Shchekinov (2013) argued that SBs created by multiple SNe in a star cluster are more effective as a feedback mechanism, in comparison to incoherent SNe. Recent simulations of interacting SNe by Vasiliev et al. (2014) show that the fractional energy retained as thermal energy in the hot ISM can be as large as $\sim$0.1–0.3 only if the explosions are spatially and temporally correlated, such that the radiative losses are effectively compensated by new explosions. SBs produced by compact star clusters are expected to satisfy this condition. In this paper, we assume that all SNe are coincident, a good approximation if the SNR, when it becomes radiative, encompasses the whole cluster. This means that SBs are a more effective feedback agent that is responsible for magnificent galactic outflows.

In addition to elucidating differences between isolated SNe and SBs, we compare various methods of injecting SN energy in numerical simulations of the ISM. Different feedback processes, such as radiation pressure, photoionization and cosmic rays, are important in explaining outflows in galaxies of different masses and redshifts (e.g. Hopkins et al. 2012 and references therein). In this paper, we only focus on the most important feedback component, namely, thermal feedback due to SNe. We find that the SN thermal energy must be deposited over a sufficiently small volume for it to create a hot bubble and to have an impact on the surroundings. For a large energy deposition radius, the cooling time is shorter than the thermalization time-scale and thermal feedback is artificially suppressed. Most early implementations of SN feedback suffered from this problem (see Gerritsen 1997 and references therein).

The formation of a low-density bubble is essential for thermal SN feedback to work because the energy of subsequent SNe is deposited in the low-density bubble and is not radiated instantaneously; cooling is only restricted to the outer shock. While this fact has been appreciated (e.g. Gnedin 1998; Joung & Mac Low 2006), we present quantitative conditions for the formation of a strong shock and a hot, dilute bubble for different thermal feedback prescriptions. The main culprit responsible for the inefficacy of thermal feedback, in both Eulerian (e.g. Tasker & Bryan 2006; Dubois & Teyssier 2008) and Lagrangian (Springel & Hernquist 2003; Stinson et al. 2006) simulations, is the lack of resolution. In reality, a SN affects its surroundings starting at small ($\ll$1 pc) scales, by launching very fast ejecta ($\sim 10^4$ km s^{-1}) into the ISM (e.g. Chevalier 1977). Simulations in which SN energy is not deposited at small enough scales have to resort to artificial measures (turning off cooling for several energy injection time-scales, depositing energy into an artificial 'hot' phase that does not cool, etc.) in order for feedback to have any impact at all on the ISM (e.g. Gerritsen 1997; Springel & Hernquist 2003; Dubois & Teyssier 2008). These measures are necessary for including the effects of SN heating in large-scale simulations.

The continuous injection of mass and energy by SNe deep within the hot SB is expected to launch a steady wind (as first calculated by Chevalier & Clegg 1985, hereafter CC85). CC85 obtained analytical solutions for a superwind, assuming a constant thermal energy and mass input rate with an injection radius. By modelling realistic SNe as fast moving ejecta within SBs, we show that a steady CC85 wind is obtained only if a large number of SNe ($\gtrsim 10^4$) explode within the star cluster. For a smaller number of SNe, the kinetic energy of an individual SN is not thermalized within a small injection radius and there is an unsteady outflow. This should have implications for works that simply assume a CC85 wind within the SB.

In this paper, we present analytical results that can be readily used for the numerical implementation of thermal feedback using various methods. These analytical criteria are verified and extended using idealized numerical simulations. The fundamental difference between isolated SNe and SBs (i.e. the former is ineffective on galactic scales) is highlighted.

The paper is organized as follows. In Section 2, we describe various ways of implementing thermal feedback due to SNe. In Section 3, we describe the numerical set-up used to study SNe and SBs. In Section 4, we present different analytical criteria for feedback to work with a range of feedback prescriptions. We also derive the conditions for obtaining a thermalized CC85 wind within a SB. In Section 5, we present one-dimensional numerical simulations of different feedback methods with and without cooling, and we compare the results with our analytical estimates. We also briefly discuss the effects of magnetic fields and thermal conduction. In Section 6, we discuss the implications of our results for galaxy formation, feedback simulations and galactic wind observations.

2 ISM AND SUPERNOVA FEEDBACK PRESCRIPTIONS

Although the ISM is multiphase and extremely complex, for simplicity we consider a uniform, static model with a given density (typically $n = 1$ cm^{-3}) and temperature (10^4 K, corresponding to the warm ISM). We do not consider stratification because the disc scaleheight is typically a few 100 pc and the fizzling of SN feedback is essentially a small-scale problem. Moreover, the scales of interest (hundreds of pc; a few Myr) are much larger than the cluster size and the local ISM/circumstellar inhomogeneities.

For simplicity, we also assume that all SNe explode at $r = 0$. This is a good approximation because the size of a typical (super)star cluster is smaller than the bubble size at the beginning of the radiative phase.

The SN prescriptions that we consider in our analytical estimates and numerical simulations cover the full range of methods used in the literature, as follows.

(i) Kinetic explosion (KE) models. In these models, the SN energy ($E_{\rm ej}$, chosen to be 1 Bethe $\equiv 10^{51}$ erg) is given to a specified ejecta mass ($M_{\rm ej}$, chosen to be 1 M$_\odot$) distributed uniformly with an ejecta density $\rho_{\rm ej} = 3M_{\rm ej}/(4\pi r_{\rm ej}^3)$ within an ejecta radius $r_{\rm ej}$. The ejecta velocity is homologous with $v_{\rm ej}(r) = v_0(r/r_{\rm ej})$ within the ejecta; the normalization is such that the kinetic energy of the ejecta is $E_{\rm ej}$; that is, $v_0 = (10E_{\rm ej}/3M_{\rm ej})^{1/2}$. The ejecta temperature is taken

to be small ($T_{\rm ej} = 10^4$ K). After every (fixed) SN injection time $t_{\rm SN}$, the innermost $r_{\rm ej}$ of the volume is overwritten by the ejecta density and velocity, thereby pumping SN energy into the ISM. After the reverse shock propagates towards the bubble centre, once the swept-up mass is comparable to the ejecta mass, the bubble density structure is fairly insensitive to the ejecta density distribution (Truelove & McKee 1999). This model most closely resembles a physical SNR in the early stages at small ($\ll$1 pc) scales when the SN 'piston' at large speed rams into the ISM. This prescription is not widely used in galaxy formation simulations (although there are some exceptions, e.g. Tang & Wang 2005).

(ii) Thermal explosion (TE) models. In these models, the energy is deposited within the ejecta radius in the form of thermal energy at an interval of $t_{\rm SN}$. There are two variants of this model. In one class, the mass and internal energy densities are overwritten within the ejecta radius ($r_{\rm ej}$) such that the uniformly distributed ejecta thermal energy is $E_{\rm ej}$ (1 Bethe) and the uniformly distributed ejecta mass is $M_{\rm ej}$ (1 $\mathrm{M}_\odot$). We call these models thermal explosion overwrite (TEo) models, and they behave like KE models. In the second class of models, we add (in contrast to overwrite) the ejecta mass (with uniform density) to the pre-existing mass and the ejecta thermal energy (distributed uniformly) to the pre-existing internal energy within $r_{\rm ej}$. We refer to these models as thermal explosion addition (TEa) models. There are significant differences between the TEa and TEo/KE models in the presence of cooling, because TEa ejecta can become radiative if thermal energy is added to a dense ISM. Most models in the literature are analogous to TEa models with some variations (e.g. Katz 1992; Joung & Mac Low 2006; Creasey, Theuns & Bower 2013); some works such as Stinson et al. (2006), Thacker & Couchman (2000) and Agertz, Teyssier & Moore (2011) unphysically turn off cooling for some time for SN feedback to have an impact. Sometimes, all the SN energy is deposited in a single grid cell (e.g. Tasker & Bryan 2006) or in a single particle (e.g. the SN particle method in section 3.2.4 of Gerritsen 1997).

(iii) Luminosity-driven (LD) models. As discussed earlier, for typical IMFs, the mechanical energy input due to OB stars per unit time is roughly constant. This motivates a model in which internal energy and mass within an injection radius (denoted by $r_{\rm ej}$) increase at a constant rate corresponding to internal energy $E_{\rm ej}$ and mass $M_{\rm ej}$ for each SN. Some of the works that use this prescription are CC85, Mac Low et al. (1989), Suchkov et al. (1994), Mac Low & Ferrara (1999), Strickland & Stevens (2000), Cooper et al. (2008), Roy et al. (2013), Recchi & Hensler (2013) and Palouš et al. (2013).

All our models are identified with the number of OB stars $N_{\rm OB}$ (which equals the number of SNe in the star cluster) or luminosity $L_{\rm ej} = E_{\rm ej}/t_{\rm SN} = N_{\rm OB}E_{\rm ej}/t_{\rm OB}$, where $t_{\rm OB}$ is the lifetime of the OB association (taken to be 30 Myr) and $t_{\rm SN} = t_{\rm OB}/N_{\rm OB}$ is the time interval between SNe. We note that the overwrite models do not strictly conserve mass and energy. While the SN energy is much larger than the overwritten thermal energy, we need to choose a small enough ejecta radius such that the overwritten mass is subdominant relative to the ejecta mass. The explosion models are substantially slower compared to the smooth LD models because of very high temperatures created because of sudden energy injection in the former.

3 NUMERICAL SET-UP

In this section, we describe the numerical set-up corresponding to our one-dimensional simulations discussed in Section 5. Our numerical simulations use the ISM set-up and the various feedback prescriptions described in Section 2. The ISM density and temperature are chosen to be 1 cm^{-3} and 10^4 K, respectively, unless specified otherwise. The mean mass is $\mu = 0.62$ per particle and $\mu_{\rm e} = 1.17$ per electron. The initial density and temperature are uniform, and the velocity is zero.

We use the grid-based ZEUS-MP code in spherical, one-dimensional geometry (Hayes et al. 2006) to solve the standard Euler equations with source terms mimicking SN energy/momentum/mass injection for the chosen feedback model, and a sink term in the internal energy equation representing radiative cooling. Our equations are similar but not identical to equations (20)–(22) of Roy et al. (2013).[1] We note that the ZEUS code does not conserve energy to the machine precision. However, we have confirmed that energy conservation holds to better than 90 per cent in most of our runs. In fact, the Sedov–Taylor blast wave in one-dimensional spherical coordinates is one of the standard test problems presented by Hayes et al. (2006); the numerical results match the analytical solutions very closely. While most of our runs are hydro, in Section 5.4.5 we briefly discuss runs with simple models of magnetic fields and thermal conduction; various parameters for these runs are discussed there.

The radial velocity is set to zero at the inner radial boundary and other fluid variables are copied in the ghost cells. Outflow boundary conditions are applied at the outer radial boundary. Note that the outer boundary is out of causal contact. Because the set-up produces strong shocks, we use the standard ZEUS artificial viscosity to prevent unphysical oscillations at shocks (Stone & Norman 1992). The CFL number of 0.2 is found to be more robust compared to the standard value of 0.5, and is used in all the simulations.

The cooling function that we use is the collisional-ionization-equilibrium based solar metallicity table of Sutherland & Dopita (1993), with the cooling function set to zero below 10^4 K. The cooling step is implemented via operator splitting using the semi-implicit method of Sharma, Parrish & Quataert (2010). Cooling is subcycled and the number of subcycles is limited to be less than 100.

Most of our runs use a 1024 resolution grid extending from 1 pc to 2 kpc. A logarithmically spaced grid is used to better resolve smaller radii; there are equal numbers of grid points covering 1 pc to $\sqrt{2000}$ pc and $\sqrt{2000}$ pc to 2 kpc. Some runs with stronger SN feedback use a larger spatial extent (see $N_{\rm OB} = 10^6$ runs in Fig. 3), and some uniform very high-resolution runs (16 384 grid points; see Fig. 5) use a smaller extent (1–200 pc). All our simulations (except the very high-resolution simulations that are run for 3 Myr) are run for 30 Myr, which is the typical age of a young star cluster.

4 ANALYTICAL CRITERIA

In this section, we present the analytical criteria that need to be satisfied so that the various feedback models discussed in Section 2 can work. These analytical estimates help us to understand the results of the numerical simulations discussed in Section 5. While radiative cooling is the most discussed phenomenon in the context of fizzling SN feedback, the feedback prescription should satisfy additional constraints for the energy input to couple realistically with the ISM. A recurring concept in what follows is that of thermalization (i.e. in

[1] The difference from Roy et al. (2013) is that the mass and energy source terms are not uniform in time. Moreover, different feedback heating prescriptions use different source terms (e.g. KE models use a momentum source term rather than a source term in the internal energy equation).

order to be effective, the input energy should have time to couple to the ISM before it is radiated or is overwritten). In Section 4.3, we show that a steady superwind within a SB, as envisaged by CC85, occurs only if the number of SNe is sufficiently large.

In the following sections, we derive upper limits on the ejecta radius within which the feedback energy must be deposited for it to be effective. We can easily convert this radius limit into a critical mass resolution needed in smooth particle hydrodynamics (SPH) simulations; that is, $n_{\rm nbr} m_{\rm crit} \approx (4\pi/3)\rho r_{\rm crit}^3$, where ρ is the ISM density, $n_{\rm nbr}$ is the number of neighbours used in the SPH smoothing kernel and $m_{\rm crit}$ is the maximum SPH gas particle mass required for feedback to work.

4.1 Energy coupling without cooling

4.1.1 Ejecta radius constraint for overwrite models

In models where energy within the ejecta radius is overwritten (KE, TEo) the ejecta radius should be smaller than a critical radius ($r_{\rm ej} \lesssim r_{\rm crit}$) for the input energy to be coupled to the ISM. The critical radius equals the Sedov–Taylor shock radius at $t_{\rm SN}$,[2] the time lag between SNe,

$$r_{\rm crit} \equiv \left(\frac{E_{\rm ej} t_{\rm SN}^2}{\rho}\right)^{1/5} \approx 50\,{\rm pc}\, n^{-1/5} E_{\rm ej,51}^{1/5} t_{\rm SN,0.3}^{2/5}, \quad (1)$$

where $\rho(n)$ is the ISM (number) density (assuming $\mu = 0.62$), $E_{\rm ej,\,51}$ is the ejecta energy in units of 10^{51} erg and $t_{\rm SN,\,0.3}$ is the time between consecutive SNe in units of 0.3 Myr. If the ejecta radius is larger than this value, then the ejecta energy is overwritten before it can push the outer shock. Thus, in such a case, the input SN energy is overwritten without greatly affecting the ISM.

4.1.2 Sonic constraint

For thermal SN feedback to launch a strong shock, the energy should be deposited over a small enough volume, such that the post-shock pressure is much larger than the ISM pressure. This is equivalent to demanding that the outer shock velocity be much larger than the sound speed in the ISM. The shock velocity ($v_{\rm OS} \equiv {\rm d}r_{\rm OS}/{\rm d}t$, where $r_{\rm OS}$ is the outer shock radius), expressed in terms of the shock radius in the Sedov–Taylor stage, is $v_{\rm OS} \approx 0.4 E_{\rm ej}^{1/2} \rho^{-1/2} r_{\rm OS}^{-3/2}$ for an isolated SN and $v_{\rm OS} \approx 0.6 L_{\rm ej}^{1/3} \rho^{-1/3} r_{\rm OS}^{-2/3}$ for a LD SB (Weaver et al. 1977). The condition for a strong shock for an isolated SN is ($v_{\rm OS} \lesssim a_T$, where a_T is the ISM isothermal sound speed)

$$r_{\rm ej} \lesssim 174\,{\rm pc}\, E_{\rm ej,51}^{1/3} n^{-1/3} T_4^{-1/3} \quad (2)$$

and for a SB is (see equation 3 in Silich et al. 2009)

$$r_{\rm ej} \lesssim 1.5\,{\rm kpc}\, L_{\rm ej,38}^{1/2} n^{-1/2} T_4^{-3/4}. \quad (3)$$

Here, $L_{\rm ej,38}$ is the ejecta luminosity ($L_{\rm ej} = E_{\rm ej}/t_{\rm SN}$ for explosion models) in units of 10^{38} erg s^{-1} (which corresponds to $N_{\rm OB} = 100$ over $t_{\rm OB} = 30$ Myr) and T_4 is the ISM temperature in units of 10^4 K.

The sonic constraint ($v_{\rm OS} \lesssim a_T$) is typically less restrictive than the compactness requirements due to cooling in a dense ISM (see the next section). Tang & Wang (2005), who considered SN feedback in the hot ISM ($\sim 10^7$ K) of galaxy clusters and elliptical galaxies, found that the shock can quickly (when the outer radius is only $\approx$20 pc; see equation 2) decelerate to attain the sound speed in the hot ISM. After this, the outer shock propagates as a sound wave. While the sound wave can spread the SN energy over a larger radius ($\propto t$ for a sound wave, unlike a strong blast wave in which $r_{\rm OS} \propto t^{2/5}$), energy dissipation is not as efficient as in shocks.

4.2 Energy coupling with cooling

4.2.1 Luminosity-driven model

In LD models, SN feedback does not fizzle out (in fact, the shock can get started) only if the cooling rate is smaller than the energy deposition rate, that is, $3L_{\rm ej}/4\pi r_{\rm ej}^3 \gtrsim n^2\Lambda$ [$\Lambda(T)$ is the cooling function], or

$$r_{\rm ej} \lesssim 20\,{\rm pc}\, L_{\rm ej,38}^{1/3} n^{-2/3} \Lambda_{-22}^{-1/3}, \quad (4)$$

where Λ_{-22} is the cooling function in units of 10^{-22} erg cm^3 s^{-1}.

4.2.2 Thermal explosion addition model

The above criterion (equation 4) for the LD models is quite different from the criterion that we now derive for the widely used TE models with energy and mass addition (TEa model in Section 2). Because energy is added to the (possibly dense) pre-existing medium, cooling in this model can be substantial. In contrast, because the ejecta density is low, cooling losses are smaller in the overwriting models (KE, TEo). For TEa models, to launch a shock, radiative losses over the time-scale in which the shock from a point explosion reaches the ejecta radius,

$$t_{\rm ej} = E_{\rm ej}^{-1/2} r_{\rm ej}^{5/2} \rho^{1/2}, \quad (5)$$

should be smaller than the energy deposited (here, ρ is the density of the medium in which energy is injected, not necessarily the ISM density); i.e.

$$n^2 \Lambda t_{\rm ej} \lesssim 3E_{\rm ej}/4\pi r_{\rm ej}^3. \quad (6)$$

Inserting the expression for $t_{\rm ej}$, we obtain

$$r_{\rm ej} \lesssim 31\,{\rm pc}\, E_{\rm ej,51}^{3/11} \Lambda_{-22}^{-2/11} n^{-5/11}. \quad (7)$$

This condition is much more restrictive than the one obtained by replacing $t_{\rm ej}$ in equation (6) by the CFL stability time-step. Moreover, this is the appropriate time-scale to use because the relevant time-scale for the injected energy to couple to the ISM is the thermalization time ($t_{\rm ej}$).

Creasey et al. (2011) and Dalla Vecchia & Schaye (2012) have used similar arguments and have derived results not too different from ours for the TEa models. A slight difference from our work is that they consider energy deposition over a resolution element (a necessity because of a larger range of scales in cosmological galaxy simulations), but we allow for energy deposition over a resolved region. Creasey et al. (2011) have expressed their resolution limit in terms of the cooling rate per unit mass and Dalla Vecchia & Schaye (2012) in terms of the post-shock temperature; we use the cooling function (Λ) to express the critical radius within which the energy needs to be deposited.

[2] We use the Sedov–Taylor expression for the bubble radius in equation (1) because the shock quickly transitions from a free-expanding to a Sedov–Taylor state; the Sedov–Taylor radius (when the swept-up ISM mass equals the ejecta mass) is $r_{\rm ST} \equiv (3M_{\rm ej}/4\pi\rho)^{1/3} \approx 2.5\,{\rm pc}\, M_{\rm ej,\odot}^{1/3} n^{-1/3}$, much smaller than the estimate in equation (1), where $M_{\rm ej,\odot}$ is the ejecta mass in solar units.

4.2.3 *Overwrite models*

In models where the energy and mass densities are overwritten within $r_{\rm ej}$, the condition for overcoming cooling losses and launching a shock is

$$n_{\rm ej}^2 \Lambda t_{\rm ej} \lesssim \frac{3E_{\rm ej}}{4\pi r_{\rm ej}^3},$$

where ejecta number density $n_{\rm ej} = \rho_{\rm ej}/\mu m_p$ and $\rho_{\rm ej} = 3M_{\rm ej}/4\pi r_{\rm ej}^3$; note that this expression is different from equation (6) in that the ejecta density is used instead of the ISM density. The overwrite models (KE, TEo) behave quite differently from the addition (TEa, LD) models because a larger ejecta radius means a smaller density ejecta to which energy is added. Replacing the ISM density by the ejecta density in equation (5) gives $t_{\rm ej} = E_{\rm ej}^{-1/2} r_{\rm ej}^{5/2} \rho_{\rm ej}^{1/2}$, and the condition for energy thermalization is

$$r_{\rm ej} \gtrsim 0.003\,{\rm pc}\, M_{\rm ej,\odot}^{5/4} \Lambda_{-22}^{1/2} E_{\rm ej,51}^{-3/4}. \quad (8)$$

In order to avoid radiative losses, the ejecta radius should be larger than above. This early cooling of the mass loaded SN ejecta, responsible for creating cold filaments in young SNe (e.g. Chevalier & Blondin 1995), is physical (unlike the fizzling out of the energy addition models) and should reduce the energy available to drive the SN. All our simulations use an ejecta radius much greater than this limit.

4.3 Conditions for CC85 wind

CC85 found analytical solutions for a LD wind with a fixed injection radius. Luminosity injection is expected to drive both an outer shock bounding the bubble and a wind that shocks within the hot bubble at the termination shock (see fig. 1 in Weaver et al. 1977; see also the LD run in Fig. 3). In this section, we show that for a small number of SNe (see equation 11) the SN ejecta does not thermalize within the termination shock. In that case, the density inside the bubble is much lower than the CC85 wind because most SNe occur in the dilute bubble created by earlier SNe and the thermalization radius is comparable to the outer shock radius. This has important implications for the cooling and luminosity of SN ejecta.

Following Weaver et al. (1977), the outer shock radius of a LD bubble is given by $r_{\rm OS} \approx (L_{\rm ej} t^3/\rho)^{1/5}$, the velocity by $v_{\rm OS} \approx 0.6 r_{\rm OS}/t \propto t^{-2/5}$ and the post-shock pressure by $p_{OS} \approx 0.75 \rho v_{\rm OS}^2 \approx 0.27 L_{\rm ej}^{2/5} \rho^{3/5} t^{-4/5}$. Assuming a steady superwind, the ram pressure at the termination shock ($r_{\rm TS}$; the wind is assumed to be supersonic at this radius) is $\rho_{\rm TS} v_{\rm TS}^2 = \dot{M}_{\rm ej} v_{\rm TS}/(4\pi r_{\rm TS}^2)$, where $v_{\rm TS} = (2L_{\rm ej}/\dot{M}_{\rm ej})^{1/2}$ is the wind velocity, $\rho_{\rm TS}$ is the density upstream of the termination shock and $\dot{M}_{\rm ej}$ is the mass injection rate. The wind termination shock ($r_{\rm TS}$) is located where the wind ram pressure balances the bubble pressure, i.e.

$$\frac{\dot{M}_{\rm ej} v_{\rm TS}}{4\pi r_{\rm TS}^2} \approx 0.75 \rho v_{\rm OS}^2.$$

Using $v_{\rm OS} \approx 0.6 L_{\rm ej}^{1/3} \rho^{-1/3} r_{\rm OS}^{-2/3}$ and $\dot{M}_{\rm ej} = 2L_{\rm ej}/v_{\rm TS}^2$ gives

$$\frac{r_{\rm TS}}{r_{\rm OS}} \approx \left(\frac{v_{\rm OS}}{v_{\rm TS}}\right)^{1/2} \approx 0.08 E_{\rm ej,51}^{-1/12} M_{\rm ej,\odot}^{1/4} n^{-1/6} r_{\rm OS,2}^{-1/3} t_{\rm SN,0.3}^{-1/6}, \quad (9)$$

where $r_{\rm OS,\,2}$ is the outer shock radius in units of 100 pc and $t_{\rm SN,\,0.3}$ is the time between SNe normalized to 0.3 Myr (corresponding to $N_{\rm OB} = 100$); we have used $L_{\rm ej} = E_{\rm ej}/t_{\rm SN}$ and $\dot{M}_{\rm ej} = M_{\rm ej}/t_{\rm SN}$. The ratio $r_{\rm TS}/r_{\rm OS}$ depends very weakly on time ($\propto t^{-1/5}$); this comes from the time dependence of $r_{\rm OS}$ in equation (9). The reverse shock for an isolated SN very quickly (at the beginning of the Sedov–Taylor stage) collapses to a point but the termination shock for a SB is present at all times. Thus, the non-radiative termination shock can power a SB long after the outer shock becomes radiative, unlike a SN that dies off shortly after the outer shock becomes radiative (see Section 5.4.4 for our results from simulations).

The condition for the existence of a smooth CC85 wind is that the ejecta thermalization radius should be smaller than the termination shock radius. The superwind is mass loaded by previous SNe (the bubble density in the absence of mass loading is quite small because most of the mass is swept up in the outer shell). The swept-up mass up to radius r in a CC85 wind is

$$M_{\rm sw} = \int_0^r 4\pi r'^2 \rho_w(r') {\rm d}r' \approx \frac{\dot{M}_{\rm ej} r}{v_{\rm TS}} = \frac{M_{\rm ej} r}{t_{\rm SN} v_{\rm TS}},$$

where $\rho_w(r')$ is the wind density profile; here, we have assumed that the swept-up mass is dominated by the supersonic portion of the wind. Now the thermalization radius (the radius within which the deposited energy is thermalized and which should correspond to CC85's injection radius) of the ejecta is where the swept-up mass roughly equals the ejecta mass, or

$$r_{\rm th} \approx v_{\rm TS} t_{\rm SN} \approx 3\,{\rm kpc}\, E_{\rm ej,51}^{1/2} M_{\rm ej,\odot}^{-1/2} t_{\rm SN,0.3}. \quad (10)$$

Because the thermalization radius is quite large, a thermalized CC85 solution will only occur for large clusters (with shorter $t_{\rm SN}$, the time lag between SNe); for modest star clusters, the ejecta will only thermalize beyond the termination shock. Of course, the thermalization radius cannot be smaller than the size of the star cluster launching the energetic ejecta. Using equation (9) and $r_{\rm OS} \approx (L_{\rm ej} t^3/\rho)^{1/5}$, the termination shock radius can be expressed as

$$r_{\rm TS} \approx 5\,{\rm pc}\, E_{\rm ej,51}^{1/20} M_{\rm ej,\odot}^{1/4} n^{-3/10} t_{\rm SN,0.3}^{-3/10} t_{0.3}^{2/5},$$

where $t_{0.3}$ is time in units of 0.3 Myr. A CC85 solution will appear only if this termination shock radius is larger than the thermalization radius (equation 10); that is, if

$$t_{\rm SN,0.3} \lesssim 0.007 E_{\rm ej,51}^{-9/26} t_{0.3}^{4/13} n^{-3/13} M_{\rm ej,\odot}^{15/26}. \quad (11)$$

This means that $N_{\rm OB} \gtrsim 3500$ (recall that $t_{\rm SN} = t_{\rm OB}/N_{\rm OB}$, where $t_{\rm OB} = 30$ Myr is the cluster lifetime and $N_{\rm OB}$ is the number of SNe) is required for a CC85 wind to appear by 30 Myr. Thus, a thermally driven CC85 wind occurs only for a sufficiently large starburst, with a large mass loading, and at late times.

5 SIMULATION RESULTS

In this section, we present the results from our one-dimensional numerical simulations. We vary the ISM density and SN injection parameters to assess when the SN energy can significantly affect the ISM, both with and without cooling. We also numerically verify the various analytical constraints presented in Section 4. We discuss the structure of a radiative SB and compare the energetics of isolated SNe and SBs. While isolated SNe lose most of their mechanical energy by a few Myr, SBs can retain up to ∼40 per cent of the input energy long after the outer shock becomes radiative. Thus, SBs, and not isolated SNe, are the viable energy sources for global, galactic-scale feedback. In Section 5.4.5, we briefly discuss the impact of magnetic fields and thermal conduction on SBs.

5.1 Realistic SN shock (KE models)

The SN shock is launched once a protoneutron star forms at the centre of a massive evolved star (with size $\sim 10^{14}$ cm). In the

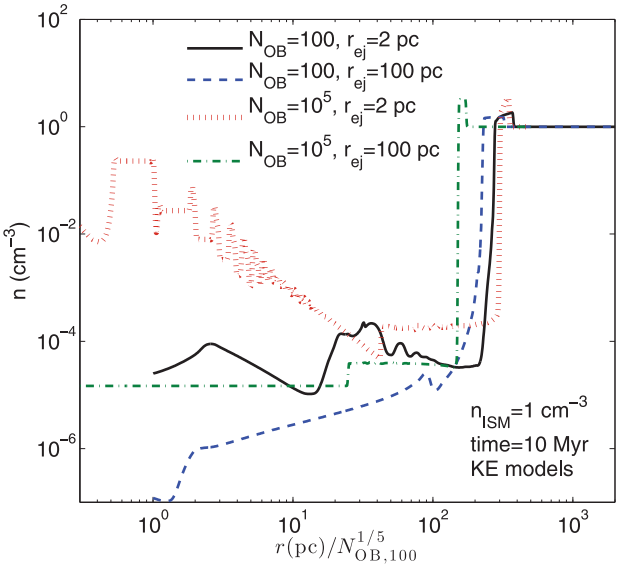

Figure 1. Number density as a function of radius (scaled to the self-similar scaling) for different parameters of realistic KE runs at 10 Myr. The outer shock is closer in for models using a larger ejecta radius because energy is overwritten before it can couple to the ISM.

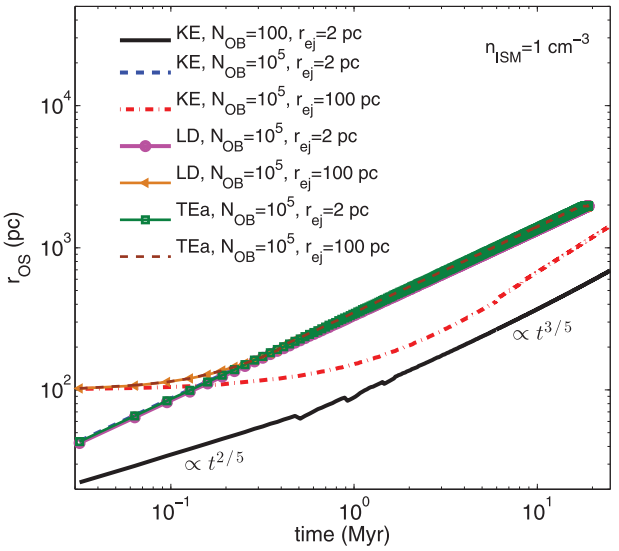

Figure 2. Outer shock radius as a function of time for various runs using KE, LD and TEa models. The KE models give correct results only if the ejecta radius ($r_{\rm ej}$) is sufficiently small; otherwise, energy is overwritten before being coupled to the ISM. There is no such problem for TEa and LD models. At early times, the outer shock radius scales with the Sedov–Taylor scaling ($r_{\rm OS} \propto t^{2/5}$) and later, after many SNe explode, it steepens ($r_{\rm OS} \propto t^{3/5}$).

ejecta-dominated state (when the swept-up ISM mass is less than the ejecta mass), the cold ejecta is dominated by kinetic energy (e.g. Truelove & McKee 1999). In our 'realistic' simulations (KE models; see Section 2) we choose that the ejecta have a constant density and a velocity proportional to the radius (homologous expansion; this is a similarity solution for the freely expanding ejecta) within the ejecta. The SN shock develops a reverse shock after sweeping up its own mass in the ISM; this slows down the ejecta and communicates the presence of the ISM to the supersonic ejecta. In this section, we compare the evolution of adiabatic (cooling is turned off) KE models with different parameters, highlighting the importance of having a small ejecta radius ($r_{\rm ej}$) even in the absence of cooling for overwrite (KE, TEo) models. We have verified that KE and TEo models behave in a similar fashion.

Fig. 1 shows the density profile as a function of radius [normalized to the self-similar scaling, $r_{\rm OS} \approx (L_{\rm ej} t^3/\rho)^{1/5}$, where $L_{\rm ej} = E_{\rm ej}/t_{\rm SN} = E_{\rm ej} N_{\rm OB}/t_{\rm OB}$] for different realistic runs (the results are similar for TEo models) with $N_{\rm OB} = 100$ and 10^5 at 10 Myr. The runs with a large ejecta radius (100 pc) give a smaller outer shock radius because most of the energy is overwritten without being thermalized (see Section 4.1.1 for a discussion). The problem is worse for larger $N_{\rm OB}$ (shorter $t_{\rm SN}$), as expected from equation (1). The normalized locations of the outer shock fall almost on top of each other for a small ejecta radius ($r_{\rm ej} = 2$ pc). As expected, the shock is weaker and broader, and has a modest density jump for a smaller number of SNe.

5.2 Comparison of adiabatic models

While the KE model is most realistic, we expect other models in Section 2 to give a similar location for the outer shock after the swept-up ISM mass equals the ejecta mass and the shock is in the Sedov–Taylor regime. The structure within the bubble depends on the SN prescription, as we show in Section 5.3.

Fig. 2 shows the location of the outer shock (measured by its peak density) as a function of time for various models (KE, LD, TEa) and SN parameters in the absence of cooling. The solid line at the bottom shows the transition from a single blast wave (outer shock radius, $r_{\rm OS} \propto t^{2/5}$) to a continuously driven bubble ($r_{\rm OS} \propto t^{3/5}$; Weaver et al. 1977) for $N_{\rm OB} = 100$ runs. The runs with more SNe show such a transition very early on. The dot-dashed line shows the outer shock radius for the KE run using a large ejecta radius violating the criterion in equation (1); the outer shock radius is much smaller than expected because energy is overwritten before it energizes the hot bubble (see Section 4.1.1). The LD and KE models agree only if the ejecta radius satisfies equation (1) for KE models (we have verified that this constraint also applies to the TEo models). The TEa runs and LD runs fall on top of each other for both choices of $r_{\rm ej}$ (2 and 100 pc). The outer shock radii for the runs with $r_{\rm ej} = 100$ pc increase only after a thermalization time (equation (5); although, in this case, ρ is not the ISM density but the much lower density of the bubble within which energy is added).

5.3 CC85 wind within the bubble

In this section, we show that a simple steady wind, as predicted by CC85, exists within the bubble only if the number of SNe is sufficiently large (see Section 4.3). Fig. 3 shows the density profile as a function of the scaled radius for various models. The solid line shows density for a LD model with $N_{\rm OB} = 100$ and $r_{\rm ej} = 2$ pc; various regions for the smooth CC85 wind within the bubble are marked. The superwind has a structure identical to the CC85 wind; the sonic point is just beyond the energy injection radius (2 pc). The wind shocks at the termination shock ($r_{\rm TS}$) where the wind ram pressure balances the bubble pressure. The ratio of the termination shock and the outer shock ($r_{\rm OS}$) is ≈0.07, in good agreement with equation (9). For comparison, Fig. 3 also shows the density profiles for the KE and TEa models with the same parameters. While the outer shock radius agree for these runs, the density profiles within the bubble are quite different. The most blatant difference, for runs with $N_{\rm OB} = 100$, is the absence of a CC85 wind in the KE and TEa models. In accordance with the discussion in Section 4.3, SN

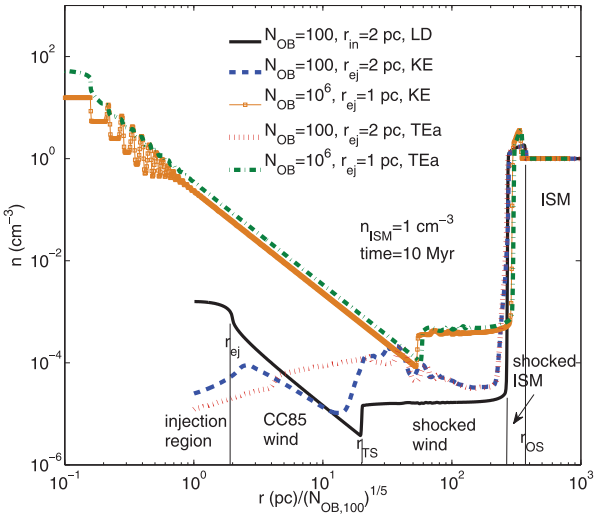

Figure 3. Density profile as a function of normalized radius for LD, KE and TEa models. The standard CC85 wind within the bubble appears for the LD model, and for KE and TEa models with $N_{\rm OB} = 10^6$, but not for KE/TEa models with $N_{\rm OB} = 100$; the smooth CC85 wind is identified by the density profile varying $\propto r^{-2}$ between the ejecta radius and the termination shock (various regions have been marked for the LD run). The CC85 wind density using $N_{\rm OB} = 10^6$ is slightly smaller for the KE model compared to the TEa model because density is overwritten (and hence mass is lost) in KE models.

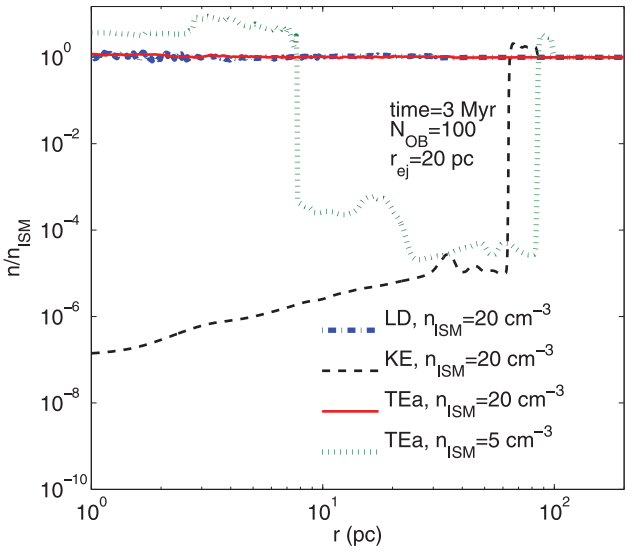

Figure 4. Density is shown as a function of radius for different runs at 3 Myr in order to show that energy addition totally fizzles out for a high ISM density. While TEa and LD models do not show the formation of a hot, dilute bubble for the ISM density of 20 cm^{-3}, the KE model indeed shows a bubble and a forward shock. Also shown is the density profile for the TEa model with a lower density (5 cm^{-3}) ISM; at later times, it shows a bubble that pushes the shell outwards. The outer shock radius is larger for a lower density ISM because $r_{\rm OS} \propto \rho^{-1/5}$.

shocks do not thermalize within the termination shock for a small number of SNe (see equations 10 and 11); therefore, a smooth CC85 wind is not expected in any model with small $N_{\rm OB}$ except for the LD model.

Only for a large enough $N_{\rm OB}$ and late enough times does a CC85 wind start to appear within the hot bubble. Fig. 3 includes the density profiles for KE and TEa models using $N_{\rm OB} = 10^6$; the inner (outer) radius of the computational domain for these runs is 0.5 pc (5 kpc), and $r_{\rm ej} = 1$ pc is chosen to satisfy the constraint in equation 1. Clearly, in these cases, we see the appearance of the CC85 wind solution within the termination shock because the injected energy is thermalized. For the KE run with $N_{\rm OB} = 10^6$, we can still see the internal shocks due to isolated SNe interacting with the superwind. The density profile for the KE model using $N_{\rm OB} = 10^5$ is shown by the dotted line in Fig. 1. In agreement with equation (9), the ratio $r_{\rm TS}/r_{\rm OS}$ increases with an increasing $N_{\rm OB}$. For $N_{\rm OB} = 10^5$, thermalization is less complete compared to $N_{\rm OB} = 10^6$, but occurs within the termination shock. In comparison, a clear termination shock is absent for $N_{\rm OB} = 100$ because the thermalization radius is larger than the termination shock radius (see equation 11).

5.4 Effects of radiative cooling

In this section, we study the effects of radiative cooling on SNe and SBs. We focus on a few aspects: the fizzling out of thermal feedback in some models in which energy is not injected over a sufficiently small scale; the comparison of cooling losses and mechanical energy retained by radiative SNRs and SBs; the influence of magnetic fields and thermal conduction.

5.4.1 Unphysical cooling losses with thermal energy addition

As mentioned in Section 4.2, some models (TEa, LD) in which we add SN thermal energy in a dense ISM, over a large radius, can suffer unphysical catastrophic radiative cooling. In such cases, a hot bubble is not even created and SN feedback has no effect, whatsoever. Early SN feedback simulations suffered from this problem because of low resolution.

Fig. 4 shows the density profiles at 3 Myr for three of our energy injection models (KE, LD, TEa) with $N_{\rm OB} = 100$ and the ISM density of 20 cm^{-3}. The ejecta radius is chosen to be large such that it violates conditions in equations (4) and (7). The figure shows a comparison of the LD and TEa models that fizzle out and the KE model, which shows a hot, dilute bubble. Thus, our results are in agreement with the analytical considerations of Section 4.2. The outer shock location for the KE model roughly agrees with the self-similar scaling of Weaver et al. (1977) if the luminosity is reduced by a factor of $\approx$0.35; this is comparable to the fraction of mechanical energy retained by SBs after the outer shock becomes radiative (see Section 5.4.4 and the right panel of Fig. 8).

For most runs in Fig. 4 we have chosen a rather high density ($n = 20\,{\rm cm}^{-3}$) compared to the critical values in equations (4) and (7). For lower densities (e.g. 5 cm^{-3} for the TEa model in Fig. 4), we find that the energy does not couple at early times. Energy injection excites large amplitude sound waves and associated density perturbations, such that at late times the lowest density regions no longer violate equations (4) and (7). After this, a hot bubble starts to grow because of energy injection in a dilute medium (see the dotted line in Fig. 4), and eventually the outer shock radius starts to agree with analytical estimates.

5.4.2 SB evolution with cooling

In this and later sections, where we study the influence of radiative cooling on SBs and SNRs, we use the realistic KE model for SN energy injection with ejecta radius $r_{\rm ej} = 2$ pc. However, we have verified that other models discussed in Section 2 give similar results, as long as the conditions in Section 4 are satisfied.

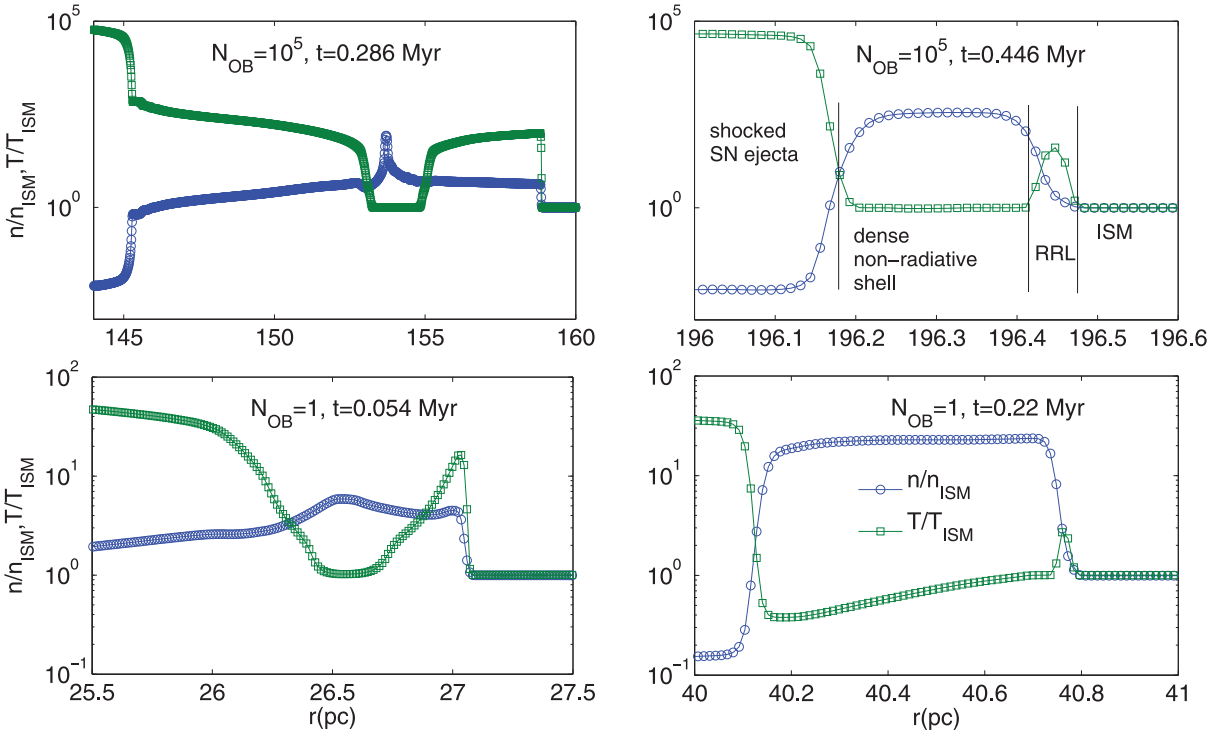

Figure 5. Normalized (with respect to the ISM) density and temperature profiles zoomed in on the outer shock as a function of radius for the high-resolution (16 384 grid points uniformly spaced from 1 to 200 pc) runs. The top panel shows the $N_{\rm OB} = 10^5$ run and the bottom panel shows a single SNR ($N_{\rm OB} = 1$) run. Left panels correspond to a time when the outer shocks just become radiative and the right panels are for later times. Markers represent the grid centres. For a single SNR, the temperature in the dense shell is lower than the temperature floor (ISM temperature) because of weakening of the shock and the resultant adiabatic losses. Different regions (unshocked ISM, radiative relaxation layer, dense non-radiative shell and shocked SN ejecta) are marked in the top-right panel.

Spherical adiabatic blast waves, both SNRs and SBs, have shells with finite thickness. An estimate for the shell thickness is obtained by assuming that all the swept-up ISM mass lies in a shell and that the post-shock density is four times the ISM density for a strong shock; this gives $\Delta r/r_{\rm OS} \approx 1/12$. Of course, the shock transition layer is unresolved in simulations, and in reality is of the order of the mean free path. The structure of an adiabatic blast waves is fairly simple. The density jump at the shock is 4 for a strong shock, and as the shock becomes weaker the density jump decreases and the shell becomes broader. Eventually, the outer shock is so weak that it no longer compresses gas irreversibly, but instead becomes a sound wave with compressions and rarefactions (see fig. 2 in Tang & Wang 2005).

Because the evolution of isolated SNRs with cooling has been thoroughly studied in the past (e.g. T98), we only highlight the differences between isolated SNRs and SBs. The fundamental difference between the two is that SNRs suffer catastrophic losses just after they become radiative, because, unlike in SBs, there is no energy injection after this stage. In SBs, the cool (yet dilute), fast SN ejecta periodically thermalize within the bubble and power it long after the forward shock becomes radiative. This keeps the radiative forward shock moving (like a pressure-driven snowplough), as long as SNe explode within the hot bubble.

The structure of a radiative shell is quite complex. The shell become radiative when the cooling time of the post-shock gas is shorter than its expansion time (which is of the order of the age of the blast wave). Moving inward from the upstream ISM, the outer shock transition occurs over a mean free path, which is followed by a thin radiative relaxation layer of the order of the cooling length (see, for example, Shu 1992, pp. 226–229, and the top-right panel of Fig. 5). The radiative relaxation layer is followed by a dense shell, which is separated by a contact discontinuity from the dilute hot bubble. In the steady state, radiative cooling is concentrated at two unresolved boundary layers: the outer radiative relaxation layer and the inner contact discontinuity. Here, the density is high and the temperature is conducive to radiative cooling.

Fig. 5 shows zooms of the density and temperature structure of the radiative shell for a SB (with $N_{\rm OB} = 10^5$; upper panels) and a SNR ($N_{\rm OB} = 1$; lower panels) using high-resolution (with 16 384 grid points) runs. It clearly shows an outer radiative shock and an inner contact discontinuity. Within the contact discontinuity of the SB ($N_{\rm OB} = 10^5$) is the shocked SN ejecta; Fig. 3 shows the full structure of a superwind within the SB. Just when the outer shock becomes radiative, the coolest/densest part is compressed by high-pressure regions sandwiching it (left panels of Fig. 5). After a sound crossing time, the post-shock region is roughly isobaric and in the pressure-driven snowplough phase (right panels of Fig. 5).

Unlike SBs, for isolated SNRs there is no energy injection at later times; the pressure in the bubble falls precipitously after the outer shock becomes radiative at ≈0.05 Myr. By ∼0.5 Myr, the bubble pressure becomes comparable to the ISM pressure, the shell density falls and it becomes momentum conserving with a velocity comparable to the sound speed in the ISM. At even later times (∼a few Myr) the hot bubble just oscillates as a weak acoustic wave.

Fig. 6 shows the distribution of radiative losses in the shell and in the bubble (a shell is defined as the outermost region where density is above 1.01 times the ISM density; a bubble comprises all the grid

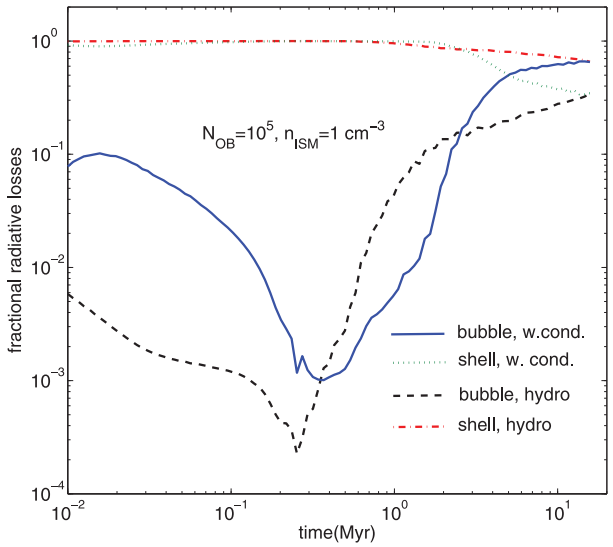

Figure 6. Fractional radiative losses in the shell [(shell cooling rate)/(total cooling rate)] and bubble [(bubble cooling rate)/(total cooling rate)] for KE models ($N_{OB} = 10^5$) with and without conduction (the run with thermal conduction is discussed in Section 5.4.5). Most radiative energy losses occur at the radiative relaxation layer ahead of the dense shell. At late times, as the outer shock weakens, radiative losses in the bubble become more dominant. The bubble is comparatively more radiative (in fact, bubble losses exceed shell losses after 5 Myr) with conduction because of mass loading of the bubble by evaporation from the dense shell. Results from the high-resolution run and the LD model are similar. The minimum in fractional radiative losses corresponds to the time when the outer shock becomes radiative.

points with a radius smaller than the inner shell radius) for a SB with $N_{OB} = 10^5$; results from runs with and without thermal conduction are shown. Here, we only discuss the run without conduction; the run with conduction is highlighted in Section 5.4.5. Unlike Fig. 5, here we use our standard resolution runs (1024 grid points) because we are running for a much longer time. Results from the higher-resolution runs match our standard runs, highlighting the fact that the volume-integrated cooling is the same even if the radiative relaxation layer and the contact discontinuity are unresolved. The time- and volume-integrated losses ($\iint n^2 \Lambda 4\pi r^2 \mathrm{d}r\, \mathrm{d}t$) in the bubble and shell are sampled appropriately and differentiated in time to obtain their respective cooling rates. As already discussed, cooling is concentrated at the radiative relaxation layer, which is included in the shell, and at the contact discontinuity, part of which is included in the bubble. Consistent with our previous discussion, most radiative losses are concentrated in the shell. Fractional radiative losses in the bubble (concentrated at the contact discontinuity) are $\sim 10^{-4}$–0.3, which increase with time as the outer shock becomes weaker.

5.4.3 *Scales in radiative shocks*

The structure of a radiative shock is well known (e.g. Shu 1992, pp. 226–229). Applying mass and momentum conservation across the radiative relaxation layer in the shock frame, and assuming the same temperature upstream/downstream of it (see the top-right panel of Fig. 5 for different regions of the outer shock) gives $\rho_3/\rho_1 = (u_1/u_3) = (u_1/a_T)^2$ (equation 16.36 in Shu 1992), where ρ_3 (ρ_1) is the density downstream (upstream) of the radiative relaxation layer, u_1 (u_3) is the upstream (downstream) velocity in the shock rest frame and a_T is the isothermal sound speed of upstream ISM (at $T = 10^4$ K, below which radiative cooling vanishes). Thus, we expect a larger density jump across stronger shocks ($u_1 \gg a_T$). This is evident from the shell density for the two cases ($N_{OB} = 10^5$ and 1) in Fig. 5.

The thickness of the cold, dense shell can be estimated by equating the swept-up ISM mass with the mass in the constant density shell; $\Delta r/r_{OS} \approx (a_T/u_1)^2/3$. This thickness is quite small, with $\Delta r/r_{OS} \approx 0.003$ for a 100 km s^{-1} shock. This estimate agrees with our results in Fig. 5 and, as predicted, the shell is thicker for a smaller N_{OB} and becomes thicker with time as the shock becomes weaker.

The thickness of the radiative relaxation layer can also be estimated. The size of the radiative relaxation layer is L_{cool} (where L_{cool} is the distance behind the outer shock after which the advection time becomes longer than the cooling time), such that

$$\int_0^{L_{cool}} \frac{\mathrm{d}x}{u} = \int_0^{t_{cool}} \mathrm{d}t = t_{cool}, \tag{12}$$

where $u(x)$ is the velocity in the relaxation layer in the shock rest frame. While this equation can only be solved after numerically solving for the structure of the relaxation layer, we can make an order of magnitude estimate. The integral on the left-hand side of equation (12) can be estimated as $L_{cool}/\langle u \rangle$, where $\langle u \rangle = a_T/2$ is the geometric mean of the velocity at the front of the relaxation layer ($u_1/4$ for a strong shock) and just downstream of it ($u_3 = a_T^2/u_1$). Similarly, the cooling time t_{cool} in equation (12) can be estimated by using a geometric mean of densities across the relaxation layer. That is, $t_{cool} \approx 1.5kT/(\langle n \rangle \Lambda)$, where $\langle n \rangle = 2(u_1/a_T)n_1$, and we can use the peak of the cooling function for T and Λ. Putting this all together gives

$$L_{cool} \sim a_T \left(\frac{a_T}{u_1}\right) \frac{kT_0}{n_1 \Lambda_0}, \tag{13}$$

which is $\sim 10^{-4}$ pc for fiducial numbers, far from being resolved even in our highest-resolution runs. While the transition layers (contact discontinuity and radiative relaxation layer) where all our cooling is concentrated are unresolved, we find that the volume-integrated quantities, such as radiative losses and kinetic/thermal energy in shell/bubble, are converged even at our modest resolution (1024 grid points; results are similar even for 256 grid points).

5.4.4 *Energetics of radiative SBs and isolated SNRs*

In this section, we focus on the energetics of the SB shell/bubble and compare it with the results from isolated SNRs. We define the shell to be the outermost region where the density is larger than 1.01 times the ISM density. All gas at radii smaller than the shell inner radius is included in the bubble (this definition is convenient but not very precise because it includes a small contribution from the unshocked SN ejecta). Fig. 7 shows a comparison of kinetic and thermal energies in the bubble and shell as a function of time for a SB driven by 10^5 SNe. The bubble kinetic energy is not included because it is much smaller. Also included is a comparison of the same quantities for the same frequency of SNe that explode independently. The results for multiple isolated SNe are obtained by combining the single SN run at different times. We simply use the data at an interval of t_{SN} (the time between individual SNe) and add them to obtain the total kinetic/thermal energy in the shell and bubble at a given time. For instance, the thermal energy in bubbles of all independent SNe at time $10t_{SN}$ is obtained by summing up the bubble thermal energy from a single SN ($N_{OB} = 1$) run at $t = 0$,

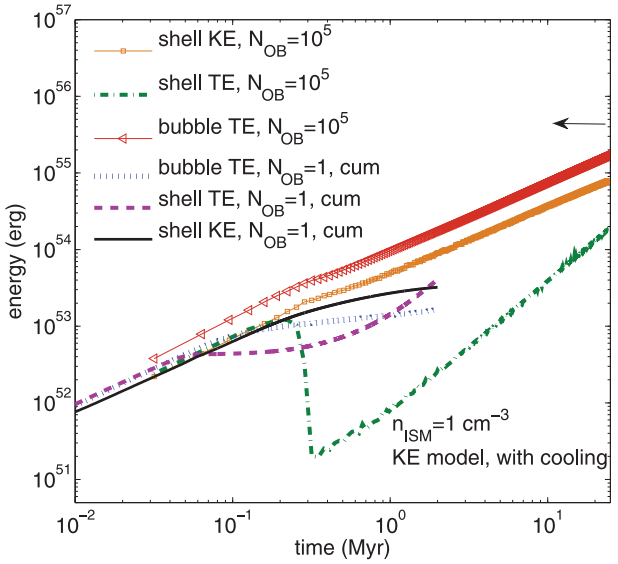

Figure 7. Comparison of kinetic and thermal energies in the shell and thermal energy in the bubble as a function of time for SBs and an equal number of isolated SNe. Results from an isolated SN run ($N_{\rm OB} = 1$) have been combined cumulatively (see equation 14), assuming that SNe explode independently in the ISM. Pre-radiative phase energetics are similar but isolated SNRs are extremely deficient in mechanical energy (after 1 Myr) compared to a SB with the same energy input. The arrow at the top-right shows the bubble thermal energy at the end for an adiabatic SB run. Isolated SN results are only shown up to 2 Myr because SNRs become weak sound waves by then.

$t_{\rm SN}$, $2t_{\rm SN}$, ..., up to $10t_{\rm SN}$. This is equivalent to a cumulative sum over time for a single SN run,

$$E_{\rm cum}(t) = \sum_{i=0}^{i<N} E(it_{\rm SN}) = \frac{1}{t_{\rm SN}} \int_0^t E(t')\,{\rm d}t', \qquad (14)$$

where E stands for, say, bubble thermal energy and N is the number of SNe up to time t.

Weaver et al. (1977) have given analytical predictions for energy in different components of SBs: the total energy of the shell is $(6/11)L_{\rm ej}t$ (40 per cent of this is kinetic energy and 60 per cent is thermal) and the thermal energy of the bubble is $(5/11)L_{\rm ej}t$ (the kinetic energy of the bubble is negligible). These analytical predictions agree well with our numerical results in the early adiabatic (non-radiative) SB phase in Fig. 7.

Fig. 7 shows that the SB shell loses most of its thermal energy catastrophically at ≈0.25 Myr; the trough in shell thermal energy can be estimated by assuming that all the swept-up mass up to then cools to the stable temperature (10^4 K). The thermal energy of the cold shell increases after that as it sweeps up mass from the ISM; this is not a real increase in the thermal energy because the newly added material, which was previously part of the ISM, simply becomes a part of the dense shell at the same temperature. The bubble thermal energy and the shell kinetic energy show only a slight decrease in slope after the radiative phase because they are energized by the non-radiative termination (internal) shock(s) driven by SN ejecta. However, there are some losses because of cooling at the contact discontinuity (see Figs 5 and 6).

The shell kinetic energy and the bubble thermal energy in radiative SB simulations at 20 Myr are roughly half of the values obtained in adiabatic simulations (which agree with analytical predictions). Thus, the mechanical energy retained in the SB is $\approx 0.34 L_{\rm ej}t$. This should be contrasted with the energy evolution in isolated SNRs. The isolated SNR becomes radiative much earlier (≈0.05 Myr; when the shell thermal energy shown by the dashed line flattens suddenly in Fig. 7) because of a weaker shock compared to a SB. Note that the energies for isolated SNe in Fig. 7 are cumulative sums over the time of a single SN run (see equation 14). The bubble thermal energy and shell kinetic energy also drop for an individual SNR after it becomes radiative, albeit not catastrophically, unlike the shell thermal energy (see fig. 3 in T98; this is the pressure-driven snowplough stage) because of cooling at the contact discontinuity and adiabatic losses, and because there is no new energy source (unlike the termination/internal shocks in a SB). The total mechanical energy in the bubble and shell of a single SNR at the beginning of the momentum conserving phase (1 Myr; when bubble pressure is comparable to the ISM pressure) is 10^{50} erg, which is only 10 per cent of the input energy (see fig. 3 in T98). This agrees with the energy fraction available as mechanical energy of the SNR, as quoted by T98. After a few Myr, the SNR should be considered a non-energetic part of the ISM, because the thermal energy of the swept-up ISM becomes larger than the SNR's mechanical energy, and the bubble becomes a weak acoustic wave.

In order to compare isolated SNRs and SBs over the cluster lifetime, we must extrapolate our cumulative SN energies to 30 Myr. This is also the relevant time-scale for preventing large-scale galactic inflows from efficiently forming stars (the free-fall time-scale at ∼10 kpc for galactic haloes is a few tens of Myr). For isolated SNRs, the shell kinetic energy + bubble thermal energy is ∼7 per cent of the input energy by 2 Myr, and only 0.7 per cent when extrapolated to 30 Myr. We should not extrapolate the shell thermal energy because its rise at late times in Fig. 7 is due to the sweeping up of the ISM into the shell, without an increase in the temperature. To conclude, isolated SN feedback is much weaker (by a factor of ∼50) compared to the feedback due to SBs over the cluster lifetime.

The left panel of Fig. 8 shows the total radiated energy over the whole computational domain as a function of time for an isolated SNR ($N_{\rm OB} = 1$; solid line) and for SBs (dashed lines). The results are qualitatively different for SBs (even for $N_{\rm OB} = 10$) and isolated SNe. While an isolated SN radiates almost all of the input energy (10^{51} erg) over a Myr time-scale, SBs radiate a smaller fraction (0.6–0.8) of their energy even up to late times. The runs with smaller $N_{\rm OB}$ and larger density become radiative at an early time because the shock is weaker, but SB runs are qualitatively similar. Unlike in isolated SNe, a significant fraction of the input energy in SBs is retained in the bubble thermal energy and the shell kinetic energy (0.2–0.4; see Fig. 7). The key reason for the difference between isolated SNe and SBs is that in SBs the non-radiative termination/internal shocks keep the bubble overpressured but isolated SNe, which do not have further energy input after the initial explosion, simply fizzle out soon after they become radiative.

The right panel of Fig. 8 shows the fraction of energy retained (1– the fraction radiated) as a function of time for several runs. All SB runs, including a higher-density run ($n_{\rm ISM} = 10$ cm^{-3}) and the run with conduction (see Section 5.4.5), show the asymptotic fraction of energy retained to be $\gtrsim$0.25. In contrast, an isolated SN loses 90 per cent of the input energy by a few Myr (and almost all of it by 10 Myr; see also Fig. 7). Radiative losses for an isolated SNR at late times ($\gtrsim$a few Myr) are more than the energy input (10^{51} erg); these come at the expense of the thermal energy of the swept-up ISM.

We can compare our results of coincident SNe with the case of multiple SNe distributed over space in a random manner. The two cases presented in Fig. 7 represent two extreme limits: spatially

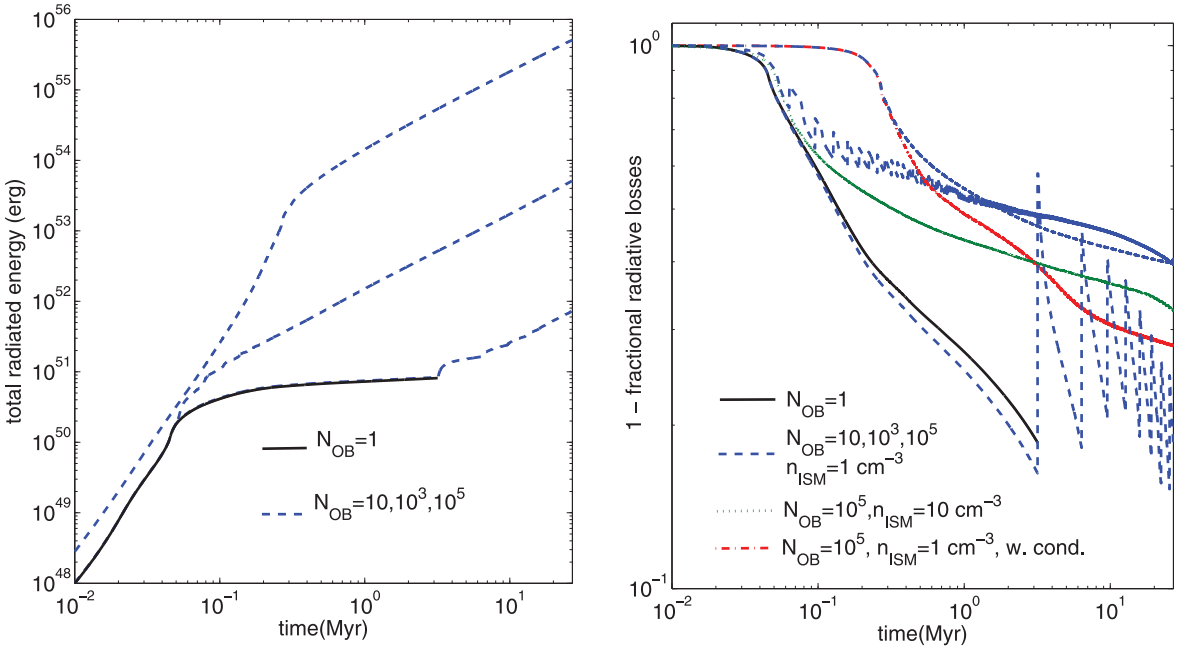

Figure 8. Radiative losses as a function of time for SBs and isolated SNe. The left panel shows the total radiated energy as a function of time for an isolated SN run (solid line) and for SB runs (dashed lines) with $N_{\rm OB} = 10$, 1000 and 10^5; larger $N_{\rm OB}$ leads to larger radiative losses because of a higher density and temperature in the radiative relaxation layer (see Fig. 5). The right panel shows fractional cooling losses, 1 − (energy radiated)/(input energy), as a function of time; the total energy input at some time equals the number of SNe put in by that time multiplied by 10^{51} erg (the spikes for $N_{\rm OB} = 10$ and 10^3 in the right panel reflect the discreteness of SN energy input within SBs). All SB runs, including those with conduction and with higher density, show that only a factor of 0.6–0.8 is radiated by 20 Myr (and a factor of 0.2–0.4 is retained as mechanical energy). In contrast, the isolated SN run (solid line) loses 80 per cent of its energy by 3 Myr, after which it is no longer overpressured with respect to the ISM.

coincident SNe in a SB and totally independent SNe. For spatially distributed SNe, we expect results somewhere in between these two extremes. Vasiliev et al. (2014) have compared the total explosion energy that remains as the thermal energy of hot gas in the case of spatially distributed SN explosions. They have studied the effects of coherent explosions, as defined by Roy et al. (2013), which implies that SNe overlap before they become radiative. If the shell radius of a SNR when it becomes radiative is R_a and the corresponding time-scale is t_a, then for a SN rate density of $\nu_{\rm SN}$, the coherency condition is that $(4\pi/3)\, R_a^3\, t_a\, \nu_{\rm SN} > 1$. Vasiliev et al. (2014) have compared the cases in which explosions occur coherently with those in which they do not. They find that a fraction ∼0.3 of the explosion energy is retained in the gas with temperature $T \geq 3 \times 10^6$ K if the explosions occur coherently, and the fraction is 0.02–0.2 if the explosions are incoherent. Our results here for SBs correspond to the coherent case, because $t_{\rm SN}$ is always shorter than the cooling time of the gas in the bubble. Therefore, our result of a fraction ∼0.35 being retained as the mechanical energy of SBs is consistent with Vasiliev et al. (2014).

5.4.5 *Effects of magnetic fields and thermal conduction*

Because the ISM is magnetized, we try to assess the qualitative effects of magnetic fields using an idealized high-resolution (16 384 grid points) MHD simulation. We assume an azimuthal (ϕ) component of the magnetic field so that only magnetic pressure forces (and no tension) are present. We choose a plasma β (ratio of gas pressure and magnetic pressure) of unity in the ISM, and our SN ejecta are also magnetized with the same value of β. Because the ejecta are dominated by kinetic energy and the bubble is expanding, we do not expect magnetic fields to affect the bubble and the ejecta structure. However, the radiative shell is compressed because of cooling, and as a result of flux-freezing, magnetic pressure is expected to build up in the dense shell. This is indeed what we find in our simulations with magnetic fields. The left panel of Fig. 9 shows the zoomed-in density and temperature structure of the radiative outer shock with and without magnetic fields. The key difference between the hydro and MHD runs is that the dense shell in MHD has a lower density and is much broader. This is because magnetic pressure prevents the collapse of the dense shell.[3] The dense shell ($194 < r < 198$ pc in the left panel of Fig. 9) is magnetically dominated with plasma $\beta \sim 0.01$. The MHD run has two contact discontinuities; one at the boundary of the hot bubble ($r \approx 191.5$ pc) and another at $r \approx 194$ pc left (right) of which the plasma is dominated by thermal (magnetic) pressure.

Another important physical effect, especially in the hot bubble, is thermal conduction. We carry out a 1024 resolution hydro run with thermal conduction to study its qualitative influence. However, it is difficult to determine the ISM conductivity in a magnetized (presumably turbulent) plasma. Therefore, we use the *Spitzer* value with a suppression factor of 0.2 (see equation 11 in Sharma et al. 2010). Moreover, because the bubble can become very hot such that the diffusion approximation breaks down, we limit the conductivity to an estimate of the free streaming diffusivity (chosen to be $2.6\, v_t r$, where v_t is the local isothermal sound speed and r is the radius). Thermal conduction is operator split, and implemented fully implicitly through a tridiagonal solver using the code's hydro time-step.

[3] The photon mean free path for a dense shell can become smaller than the shell thickness. When this occurs, the assumption of optically thin cooling breaks down, and the shell can become thicker because of radiation pressure.

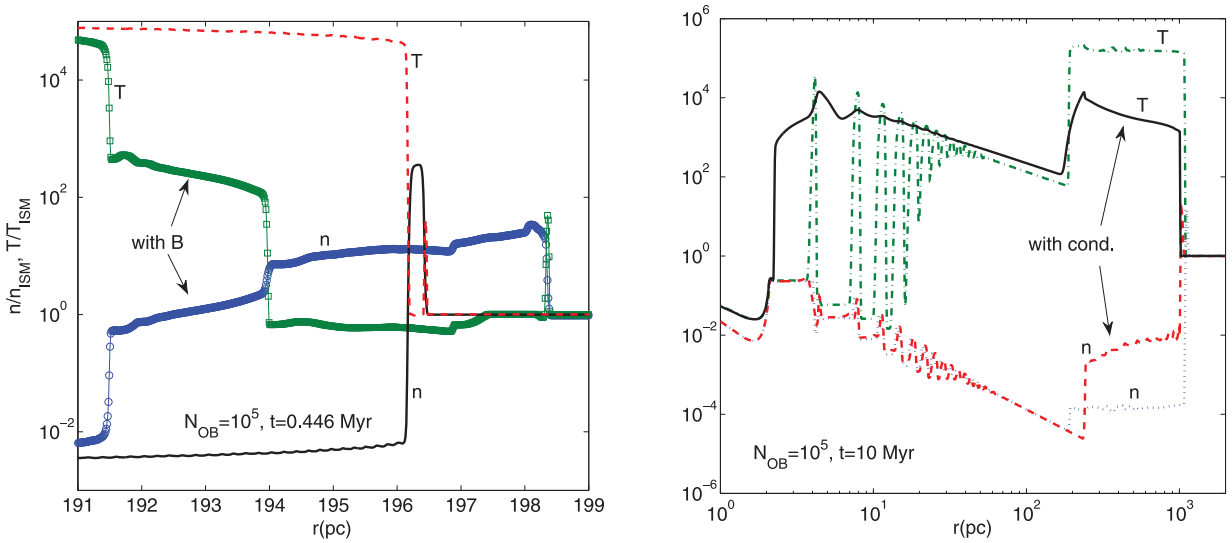

Figure 9. Normalized density and temperature profiles to show the effects of magnetic fields and thermal conduction on SB evolution with cooling. The left panel shows the profiles zoomed in on the outer shock for MHD (initial $\beta = 1$) and hydro runs with 16 384 grid points. The magnetic field is enhanced in the shell and the shell is thicker. The right panel shows the profiles for radiative hydro runs with and without thermal conduction (1024 grid points); unlike in the left panel, we show the whole computational domain and the dense shell is barely visible. Thermal conduction evaporates mass from the dense shell and spreads it into the bubble, thereby making it denser and less hot compared to the hydro run. The temperature structure in the internal shocks (within the superwind) is also smoothed out by thermal conduction.

Conduction is expected to evaporate matter from the dense shell and to deposit it into a conductive layer in the bubble; in the steady state, the rate of conductive transport of energy from the bubble to the shell is balanced by the rate of heat advection from the shell to the bubble (Weaver et al. 1977). The outer and termination shock locations are not affected much by conduction. However, the density and temperature structure in the hot bubble are affected significantly. Without conduction, the bubble is very hot ($\sim 10^9$ K), but with conduction the temperature drops into the X-ray range (10^7–10^8 K) and density is higher. This can enhance the X-ray emissivity of SBs; a rough estimate of hard X-ray luminosity ($\int 4\pi r^2 n^2 \Lambda dr$ over the hot bubble) at 10 Myr from the right panel of Fig. 9 is a few 10^{38} erg s^{-1} (which is $\sim$0.003 the energy put in by SNe by that time). Because galactic superwinds are copious X-ray emitters, we expect thermal conduction to be a very important ingredient for explaining observations. Fig. 6 confirms that the fraction of radiative losses from the bubble is much higher with conduction than without conduction because of a higher density. However, the right panel of Fig. 8 shows that the total fractional radiative losses with thermal conduction are only slightly higher compared to the non-conductive $N_{\rm OB} = 10^5$ SB run.

We emphasize that our treatment of magnetic fields and thermal conduction is extremely simplified. Realistic calculations must be done in three dimensions with tangled magnetic fields and with anisotropic thermal conduction along fields lines. However, we expect the qualitative effects of realistic magnetic fields and thermal conduction to have some semblance with our simplified treatment.

6 CONCLUSIONS AND ASTROPHYSICAL IMPLICATIONS

We have obtained several important results in this paper, both on the numerical implementation of SN/SB feedback and on the differences between isolated SNe and SBs. SBs are a result of spatially and temporally correlated SNe. Because most massive stars are expected to be born in star clusters a few tens of pc in extent (e.g. Larsen 1999), pre-SN stellar winds and the first SNe are expected to carve out a low-density bubble, which by a fraction of Myr encloses the whole star cluster (see Fig. 5). Therefore, subsequent SNe occur in the low-density bubble and we are in the SB regime of coherent SNe (see Roy et al. 2013; Vasiliev et al. 2014).

Magnificent galactic outflows, such as M82, are powered by multiple superstar clusters and the problem of understanding coalescing SBs is important. Star clusters more massive than 10^5 M$_\odot$ (and hence with >1000 SNe) are rare (e.g. Portegies Zwart et al. 2010); therefore, the SBs in M82 and in our $N_{\rm OB} = 10^5$ SB model should be considered as giant bubbles driven by hundreds of overlapping SBs due to individual star clusters. Indeed, hundreds of star clusters have been observed in the central few 100 pc of M82 (O'Connell et al. 1995). We note that vertical stratification is important for the acceleration and assimilation of the metal-rich bubble into the halo. In this paper, we consider the idealized smaller-scale problem of the behaviour of isolated SNRs and multiple coincident SNe within a SB in a uniform ISM. Some of our most important results are as follows.

(i) Our most realistic KE models (and other models in which SN energy is overwritten), in which the SN energy in kinetic form is overwritten in a small volume, give correct results only if the energy is deposited within a small length-scale (see Section 4.1.1); otherwise, energy is overwritten without coupling to the ISM. This is true even without considering any radiative losses.

(ii) With cooling, if feedback energy is deposited within a length-scale $r_{\rm ej}$ larger than the critical values mentioned in Section 4.2, such that the input energy is radiated before it is thermalized, a hot bubble is not formed in the widely used LD and TEa models. Thus, the SN fizzles out at early stages as a result of artificially large cooling losses.

(iii) With insufficient resolution and large ISM densities, the bubble fizzles out completely in the LD and TEa models (in which

energy is added to the ISM; see Section 2) and cannot have any effect on the ISM (see Fig. 4). As also pointed out previously (e.g. by Creasey et al. 2011; Dalla Vecchia & Schaye 2012), early galactic-scale SN feedback simulations failed mainly because of this. However, for a realistic SN (as mimicked by our KE model), a bubble is formed and subsequent SNe, occurring within the non-radiative bubble, power the radiative outer shock. Another, probably more serious, problem faced by numerical simulations is that the SN energy is not typically put in coherently over a small volume in space and within a short interval. Feedback due to SNe in young star clusters is expected to be coherent and much more effective than a similar number of isolated SNe (see Figs 7 and 8). For correlated SNe, isolated SN bubbles overlap to form a SB that is powered by the non-radiative termination/internal shocks, long after the outer shock becomes radiative. In contrast, an isolated SN becomes powerless just after ($\sim$1 Myr) the outer shock becomes radiative.

(iv) A smooth CC85 wind within the SB is possible only if the number of SNe ($N_{\rm OB}$) over the cluster lifetime is large (i.e. $N_{\rm OB} \gtrsim 10^4$). Only in these cases, individual SNe exploding inside the SB are able to thermalize within the termination shock. This result has implications for modelling the X-ray output, for example, in individual bubbles blown by star clusters and in the inner regions of galactic outflows, because the CC85 wind structure is often assumed where it may not be valid.

(v) Most of the radiative losses come from the unresolved radiative relaxation layer at the outer shock. The fractional radiative losses from the interior region, concentrated at the contact discontinuity between the shocked ISM and the shocked ejecta, vary between $\sim$0.001 and 0.3, with larger losses occurring at later times. While these radiative layers are unresolved even in our highest-resolution simulations, the volume-integrated radiative losses in them converge even for a modest resolution.

(vi) Compared to isolated SNe, SBs can retain a larger fraction of the initial energy of explosions as thermal/kinetic energy of the gas. Isolated SNe are mixed with the ISM soon after they become radiative; by a few Myr, they are incapable of affecting the ISM at all. While most energy is radiated away (close to 100 per cent, and not $\sim$90 per cent, as is often assumed) for isolated SNe over 10 Myr, a SB can retain a fraction $\sim$0.35 (for $n = 1\,{\rm cm}^{-3}$) as the bubble thermal energy + the shell kinetic energy. This fraction is only weakly affected by a higher ISM density and by thermal conduction (see the right panel of Fig. 8). Thus, SBs are expected to significantly affect even a dense ISM. Substantial radiative losses can partly explain the smaller observed bubble sizes compared to what is expected by modelling the stellar populations (see Oey 2009, for a summary).

(vii) The temperature profiles of SBs strongly depend on thermal conduction, whose inclusion can decrease (increase) the temperature (density) and thereby enhance the X-ray luminosity. Thermal conduction (and other sources of mass loading of the hot bubble, such as turbulent mixing) plays an important role in explaining the X-ray emission from galactic SBs because very little gas is expected to be in the X-ray emitting regime (10^6–10^8 K) in its absence (see the right panel of Fig. 9).

Our simple one-dimensional simulations show that isolated SNRs, because of large radiative losses, are much weaker feedback agents compared to SBs driven by coherently overlapping SNe. However, detailed three-dimensional calculations, particularly with a realistic distribution of stars in a cluster, and magnetic fields and thermal conduction, are required in order to make quantitative comparisons with observations. This will be done in future.

ACKNOWLEDGEMENTS

PS thanks Ramesh Narayan for useful discussions. PS is partly supported by the Department of Science and Technology of the Government of India (DST; grant no. Sr/S2/HEP-048/2012). YS is partly supported by the Russian Foundation for Basic Research (RFBR; project code 12-02-00917).

REFERENCES

Agertz O., Teyssier R., Moore B., 2011, MNRAS, 410, 1391
Chevalier R., 1974, MNRAS, 169, 229
Chevalier R., 1977, ARA&A, 15, 175
Chevalier R. A., Blondin J. M., 1995, ApJ, 444, 312
Chevalier R. A., Clegg A. W., 1985, Nature, 317, 44 (CC85)
Cooper J. L., Bicknell G. V., Sutherland R. S., Bland-Hawthorn J., 2008, ApJ, 674, 157
Cox D. P., 1972, ApJ, 178, 159
Creasey P., Theuns T., Bower R. G., Lacey C. G., 2011, MNRAS, 415, 3706
Creasey P., Theuns T., Bower R. G., 2013, MNRAS, 429, 1922
Dalla Vecchia C., Schaye J., 2012, MNRAS, 426, 140
Dubois Y., Teyssier R., 2008, A&A, 477, 79
Gerritsen J. P. E., 1997, PhD Thesis, University of Groningen
Gnedin N. Y., 1998, MNRAS, 297, 407
Guedes J., Callegari S., Madau P., Mayer L., 2011, ApJ, 742, 76
Hayes J. C., Norman M. L., Fiedler R. A., Bordner J. O., Li P. S., Clark S. E., ud-Doula A., Mac Low M.-M., 2006, ApJS, 165, 188
Hopkins P. F., Quataert E., Murray N., 2011, MNRAS, 417, 950
Hopkins P. F., Quataert E., Murray N., 2012, MNRAS, 421, 3522
Joung M. K. R., Mac Low M., 2006, ApJ, 653, 1266
Katz N., 1992, ApJ, 391, 502
Larsen S. S., 1999, A&AS, 139, 393
Leisawitz D., Bash F. N., Thaddeus P., 1989, ApJS, 70, 731
McCray R., Kafatos M., 1987, ApJ, 317, 190
Mac Low M., Ferrara A., 1999, ApJ, 513, 142
Mac Low M., McCray R., Norman M. L., 1989, ApJ, 337, 141
Nath B. B., Shchekinov Y., 2013, ApJ, 777, 12
Navarro F. F., White S. D. M., 1993, MNRAS, 265, 271
O'Connell R. W., Gallagher J. S., Hunter D. A., Colley W. N., 1995, ApJ, 446, L1
Oey M. S., 2009, in Smith R. K., Snowden S. L., Kuntz K. D., eds, AIP Conf. Proc. Vol. 1156, The Local Bubble and Beyond II. Am. Inst. Phys., New York, p. 295
Palouš J., Wünsch R., Martínez-González S., Hueyotl-Zahuantitla F., Silich S., Tenorio-Tagle G., 2013, ApJ, 772, 128
Portegies Zwart S. F., McMillan S. L., Gieles M., 2010, ARA&A, 2010, 48, 431
Recchi S., Hensler G., 2013, A&A, 551, 41
Roy A., Nath B. B., Sharma P., Shchekinov Y., 2013, MNRAS, 434, 3572
Sharma P., Parrish I. J., Quataert E., 2010, ApJ, 720, 652
Shu F. H., 1992, The Physics of Astrophysics, Vol. II, Gas Dynamics. University Science Books, Mill Valley, CA
Silich S., Tenorio-Tagle G., Torres-Campos A., Munõz-Tuñòn, Monreal-Ibero A., Melo V., 2009, ApJ, 700, 931
Springel V., Hernquist L., 2003, MNRAS, 339, 289
Springel V. et al., 2005, Nature, 435, 629
Stinson G., Seth A., Katz N., Wadsley J., Governato F., Quinn T., 2006, MNRAS, 373, 1074
Stone J. M., Norman M. L., 1992, ApJS, 80, 753
Strickland D. K., Heckman T. M., 2009, ApJ, 697, 2030
Strickland D. K., Stevens I. R., 2000, MNRAS, 314, 511
Suchkov A. A., Balsara D. S., Heckman T. M., Leitherer C., 1994, ApJ, 430, 511
Sutherland R. S., Dopita M. A., 1993, ApJS, 88, 253

Tang S., Wang Q. D., 2005, ApJ, 628, 205
Tasker E. J., Bryan G. L., 2006, ApJ, 641, 878
Thacker R. J., Couchman H. M. P., 2000, ApJ, 545, 728
Thornton K., Gaudlitz M., Janka H., Steinmetz M., 1998, ApJ, 500, 95 (T98)
Truelove J. K., McKee C. F., 1999, ApJS, 120, 299
Tumlinson J. et al., 2011, Science, 334, 948
Vasiliev E. O., Nath B. B., Bondarev R., Shchekinov Y., 2014, preprint (arXiv:1401.5070)
Weaver R., McCray R., Castor J., Shapiro P., Moore R., 1977, ApJ, 218, 377
Zhang Q., Fall S. M., Whitmore B. C., 2001, ApJ, 561, 727

This paper has been typeset from a TEX/LATEX file prepared by the author.